




# Chemical vapor deposition of tin sulfide from diorganotin(IV) dixanthates

Mundher Al-Shakban<sup>1</sup>, Peter D. Matthews<sup>2,\*</sup> , Edward A. Lewis<sup>1</sup>, James Raftery<sup>3</sup>, Inigo Vitorica-Yrezabal<sup>3</sup>, Sarah J. Haigh<sup>1</sup>, David J. Lewis<sup>1</sup>, and Paul O'Brien<sup>1,3,\*</sup>

<sup>1</sup>School of Materials, University of Manchester, Oxford Road, Manchester M13 9PL, UK

<sup>2</sup>School of Chemical and Physical Sciences, Keele University, Newcastle-under-Lyme, Staffordshire ST5 5BG, UK

<sup>3</sup>School of Chemistry, University of Manchester, Oxford Road, Manchester M13 9PL, UK

Received: 31 July 2018

Accepted: 24 September 2018

© The Author(s) 2018

## ABSTRACT

We report the synthesis and single-crystal X-ray characterization of diphenyltin bis(2-methoxyethylxanthate) and diphenyltin bis(*iso*-butylxanthate). These xanthates have been used as a single-source precursor to deposit tin chalcogenide thin films by aerosol-assisted chemical vapor deposition. Grazing incidence X-ray diffraction and scanning transmission electron microscope imaging coupled with elemental mapping show that films deposited from diphenyltin bis(*iso*-butylxanthate) contain orthorhombic SnS, while films deposited from diphenyltin bis(2-methoxyethylxanthate) between 400 and 575 °C form a SnS/SnO<sub>2</sub> nanocomposite. In synthesizing the thin films, we have also demonstrated an ability to control the band gap of the materials based on composition and deposition temperature.

## Introduction

There has recently been a surge of interest into metal chalcogenide-based materials, as these materials demonstrate a remarkable range of applications including use in magnets, catalysis, lubricants, photovoltaics, energy storage and drug delivery [1–13]. Among these, tin sulfide is a promising material that is suitable as an absorber layer for photovoltaic applications due to its exciting properties. It possesses a high absorption coefficient ( $\alpha > 10^4 \text{ cm}^{-1}$ ) [14], a band gap of 1.1–1.4 eV [15] and a theoretical power conversion efficiency of up to 24%, though so

far the record is 4.4%, leaving great room for improvement [16]. It is an attractive material for large scale use, owing to its compositional elements being earth abundant and environmentally benign. SnS in its orthorhombic form demonstrates excellent thermal stability and remains stable under ambient conditions and has found some promise as anodes in Li-ion batteries [17].

Tin is found in the second half of Group 14, and as such has two accessible oxidation states: Sn(II) and Sn(IV). As a result of a fine thermodynamic balance between divalent and tetravalent tin [18], tin sulfide can be found in three main forms: SnS [Sn(II)], Sn<sub>2</sub>S<sub>3</sub> [mixed Sn(II)/Sn(IV)] and SnS<sub>2</sub> [Sn(IV)]. The low

Address correspondence to E-mail: p.d.matthews@keele.ac.uk; paul.obrien@manchester.ac.uk

energy form of SnS is an orthorhombic herzenbergite structure, adopting a *Pnma* space group. This is a layered structure with strong Sn–S bonds in a puckered sheet and weak Van der Waals-type interactions between sheets—similar to black phosphorus [19, 20]. The mixed valent species Sn<sub>2</sub>S<sub>3</sub> also adopts the *Pnma* space group, while tetravalent SnS<sub>2</sub> is trigonal *P-3m1* [21].

Tin sulfide nanomaterials have been synthesized through a variety of ‘bottom-up’ approaches, such as chemical vapor deposition (CVD) [22–27], chemical vapor transport [18], melt reactions [28], chemical bath deposition [29, 30], colloidal nanoparticle synthesis [31–33], vacuum evaporation [34, 35], physical vapor transport [36], electrochemical deposition [37, 38], spray pyrolysis [39] or ‘top-down’ exfoliation approaches [19]. In most of the ‘bottom-up’ cases, it is difficult to produce phase-pure SnS, with mixtures of Sn<sub>2</sub>S<sub>3</sub> or SnS<sub>2</sub> often found as contaminants.

We have recently focused our attention on the use of single-source precursors to synthesize metal chalcogenide thin films and nanoparticles. In particular, we, and others, have found that simple metal xanthates [M(S<sub>2</sub>COR)<sub>x</sub>] and dithiocarbamates [M(S<sub>2</sub>CNR<sub>2</sub>)<sub>x</sub>] (R = alkyl) are excellent precursors to metal sulfides [5, 40–48]. In this report, we discuss the use of the diorganotin(IV) dixanthate complexes as precursors for the production of SnS thin films by aerosol-assisted chemical vapor deposition (AA-CVD). We focus on the annealing temperature and the role of the xanthate ligand during the decomposition process for the potential in controlling the structural and optical properties of the films produced.

## Experimental

All chemicals were purchased from Sigma-Aldrich and used without further purification. Elemental analysis of the complexes was carried out using a Flash 2000 Thermo Scientific elemental analyzer in the School of Chemistry, University of Manchester. Thermogravimetric analysis (TGA) and differential scanning calorimetry (DSC) of the complex were carried out by a METTLER TOLEDO TGA/DSC 1 star<sup>e</sup> system under an atmosphere of dry nitrogen. Scanning electron microscope images (SEM) were observed using a Philips XL 30FEG equipped with DX4 energy-dispersive X-ray spectroscopy (EDX) instrument or a FEI Quanta 200 ESEM equipped with

an EDAX Genesis V4.61 for EDX analysis. Grazing incidence X-ray diffraction (GIXRD) patterns were obtained with a Bruker D8 Advance diffractometer using a Cu-K $\alpha$  source ( $\lambda = 1.5418 \text{ \AA}$ ) and an incident angle of 3°.

Single-crystal X-ray diffraction was performed using a Bruker APEX-II CCD with a Cu-K $\alpha$  source [Ph<sub>2</sub>Sn(S<sub>2</sub>CO(CH<sub>2</sub>)<sub>2</sub>OMe)<sub>2</sub>] (1) at 100 K and a XtaLAB AFC11 (RINC): quarter-chi single with a Mo-K $\alpha$  source [Ph<sub>2</sub>Sn(S<sub>2</sub>CO<sup>*i*</sup>Bu)<sub>2</sub>] (2) at 150 K.

STEM imaging and energy-dispersive X-ray (EDX) spectroscopic analysis were performed in a probe-side aberration corrected FEI Titan G2 80-200 ChemiSTEM microscope operated at 200 kV equipped with Super-X EDX silicon drift detectors with a total collection solid angle of  $\sim 0.7$  srad. For high-angle annular dark-field (HAADF) imaging, a convergence angle of 26 mrad and a detector inner angle of 48 mrad were used. EDX spectrum images were acquired with the sample at 0° tilt and with all four of the ChemiSTEM's Super-X SDD detectors turned on. STEM images were recorded in FEI TIA software, and EDX data were recorded and analyzed using Bruker Esprit. The thicknesses of the films were measured using Veeco Dektak 8 Surface Profilometer, and the cantilever force was about 15 mg.

## Synthesis of metal xanthate complexes

### *Synthesis of potassium 2-methoxyethylxanthate [KS<sub>2</sub>CO(CH<sub>2</sub>)<sub>2</sub>OMe]*

Potassium 2-methoxyethylxanthate was prepared according to our previously published procedure [43]. Potassium hydroxide (11.2 g, 0.20 mol) was dissolved in (75 ml) of 2-methoxyethanol, the reactors were stirred for 6 h at 0 °C, and then a solution of CS<sub>2</sub> (15.2 g, 12 ml, 0.20 mol) in 2-methoxyethanol (25 ml) was added dropwise, resulting in a clear yellow solution. [KS<sub>2</sub>CO(CH<sub>2</sub>)<sub>2</sub>OMe] was isolated from solution by adding THF (100 ml) and shaking the mixture for 15 min. The yellow solid product was dried in vacuo and recrystallized from 2-methoxyethanol to give [KS<sub>2</sub>CO(CH<sub>2</sub>)<sub>2</sub>OMe] (19.8 g, 0.104 mol, 52% yield). M.p. = 216–219 °C. Calc. for C<sub>4</sub>H<sub>7</sub>KO<sub>2</sub>S<sub>2</sub> (%): C 25.3, H 3.71, S 33.6, K 20.6; found: C 25.5, H 3.79, S 33.5, K 20.8. FT-IR (cm<sup>-1</sup>): 2935 (w), 2888 (w), 1442 (m), 1445 (w), 1230 (m), 1134 (m), 1099 (m), 1066 (s), 1018 (m), 844.3 (w), 676.7 (m), 532.5 (m). <sup>1</sup>H NMR (400 MHz, D<sub>2</sub>O)  $\delta$  (ppm) = 3.35 (s, 3H,

OCH<sub>3</sub>), 3.72 (t, 2H, MeOCH<sub>2</sub>CH<sub>2</sub>OCS<sub>2</sub>), 4.50 (t, 2H, MeOCH<sub>2</sub>CH<sub>2</sub>OCS<sub>2</sub>). <sup>13</sup>C NMR (400 MHz, D<sub>2</sub>O) δ (ppm): 58.15 (OCH<sub>3</sub>), 70.2 (MeOCH<sub>2</sub>CH<sub>2</sub>OCS<sub>2</sub>), 72.1 (MeOCH<sub>2</sub>CH<sub>2</sub>OCS<sub>2</sub>), 232.5 (MeOCH<sub>2</sub>CH<sub>2</sub>OCS<sub>2</sub>).

#### Synthesis of potassium *iso*-butylxanthate [KS<sub>2</sub>CO<sup>*i*</sup>Bu]

Potassium hydroxide (5.64 g, 0.10 mol) and *iso*-butanol (50 ml) were stirred for 2 h at room temperature, and then CS<sub>2</sub> (7.73 g, 6.11 ml, 0.10 mol) was added to the reaction, resulting in an orange solution. The unreacted alcohol was removed in vacuo, and the yellow solid product was dried and recrystallized from *iso*-butanol. (9.66 g, 65% yield). M.p. = 241–243 °C. Calc. for C<sub>5</sub>H<sub>9</sub>KOS<sub>2</sub> (%): C 31.9, H 4.82, S 33.4, K 20.8; found: C 31.7, H 4.72, S 33.8, K 21.0. FT-IR (cm<sup>-1</sup>): 2958 (m), 2927 (w), 2870 (w), 1463 (w), 1386 (w), 1366 (w), 1179 (w), 1165 (w), 1141 (m), 1092 (s), 968.8 (m), 937.6 (w), 912.7 (w), 802.1 (w), 653.3 (w), 571.9 (w). <sup>1</sup>H NMR (400 MHz, D<sub>2</sub>O) δ (ppm) = 0.89 (d, 6H, CH(CH<sub>3</sub>)<sub>2</sub>), 1.99 (s, 1H, CH(CH<sub>3</sub>)<sub>2</sub>), 4.16 (d, 2H, OCH<sub>2</sub>CH).

#### Synthesis of diphenyltin bis(2-methoxyethylxanthate) [Ph<sub>2</sub>Sn(S<sub>2</sub>CO(CH<sub>2</sub>)<sub>2</sub>OMe)<sub>2</sub>] (1)

[Ph<sub>2</sub>Sn(S<sub>2</sub>CO(CH<sub>2</sub>)<sub>2</sub>OMe)<sub>2</sub>] was prepared by a procedure that was modified from that described in the literature [49]. Potassium 2-methoxyethylxanthate [KS<sub>2</sub>CO(CH<sub>2</sub>)<sub>2</sub>OMe] (0.74 g, 0.0039 mol) in ethanol (50 ml) was added dropwise to a solution of diphenyltin dichloride (0.55 g, 0.0016 mol) in DCM (50 ml) and stirred for 1 h at room temperature. After filtering, the solution was evaporated under reduced pressure and the residue was dissolved in a (1:5) DCM/ethanol solution and left to crystallize as white crystals of [Ph<sub>2</sub>Sn(S<sub>2</sub>CO(CH<sub>2</sub>)<sub>2</sub>OMe)<sub>2</sub>] (0.62 g, 0.0011 mol, 67% yield). M.p. = 186–189 °C. Calc. for C<sub>20</sub>H<sub>24</sub>O<sub>4</sub>S<sub>4</sub>Sn (%): C 41.8, H 4.21, S 22.3; found: C 41.5, H 4.21, S 22.3. FT-IR (cm<sup>-1</sup>): 3061 (w), 2935 (w), 1426 (m), 1207 (m), 1134 (m), 1052 (s), 988.2 (m), 841.3 (m), 724.3 (m), 685.9 (m), 622.3 (w), 558.2 (w). <sup>1</sup>H NMR (400 MHz, CDCl<sub>3</sub>) δ (ppm): 3.23 (s, 3H, OCH<sub>3</sub>), 3.46 (t, 2H, CH<sub>2</sub>CH<sub>2</sub>O), 4.33 (t, 2H, CH<sub>2</sub>CH<sub>2</sub>O), 7.39 (m, 3H, Ph), 7.9 (m, 2H, Ph). <sup>13</sup>C NMR (400 MHz, CDCl<sub>3</sub>) δ (ppm): 59.0 (OCH<sub>3</sub>), 69.5 (CH<sub>2</sub>CH<sub>2</sub>O), 75.0 (CH<sub>2</sub>CH<sub>2</sub>O), 129.1 (Ph), 130.2 (Ph), 135.4 (Ph), 141.3 (Ph), 218.8 (S<sub>2</sub>COCH<sub>2</sub>),

#### Synthesis of diphenyltin bis(*iso*-butylxanthate) [Ph<sub>2</sub>Sn(S<sub>2</sub>CO<sup>*i*</sup>Bu)<sub>2</sub>] (2)

[Ph<sub>2</sub>Sn(S<sub>2</sub>CO<sup>*i*</sup>Bu)<sub>2</sub>] was prepared via the same method using [K(S<sub>2</sub>CO<sup>*i*</sup>Bu)] (0.73 g, 0.0039 mol). The product crystallizes as needles crystals. (0.58 g, 0.0010 mol, 64% yield). M.p. = 92–94 °C. Calc. for C<sub>22</sub>H<sub>28</sub>O<sub>2</sub>S<sub>4</sub>Sn (%): C 46.3, H 4.94, S 22.4; found: C 46.3, H 5.28, S 22.1. FT-IR (cm<sup>-1</sup>): 3062 (w), 2960 (w), 1478 (m), 1430 (m), 1204 (w), 1154 (w), 1044 (s), 996.3 (m), 852.6 (w), 725.5 (s), 692.8 (s), 615.8 (w), 557.8 (w).

<sup>1</sup>H NMR (400 MHz, CDCl<sub>3</sub>) δ (ppm) = 0.78 (d, 6H, CH(CH<sub>3</sub>)<sub>2</sub>), 1.89 (s, 1H, CH(CH<sub>3</sub>)<sub>2</sub>), 3.98 (d, 2H, OCH<sub>2</sub>CH), 7.39 (m, 3H, Ph), 7.92 (m, 2H, Ph). <sup>13</sup>C NMR (400 MHz, CDCl<sub>3</sub>) ppm: 19.0 (CH(CH<sub>3</sub>)<sub>2</sub>), 27.6 (CH(CH<sub>3</sub>)<sub>2</sub>), 82.7 (OCH<sub>2</sub>), 129.1 (Ph), 130.2 (Ph), 135.4 (Ph), 141.6 (Ph), 225.2 (S<sub>2</sub>CO).

#### Aerosol-assisted chemical vapor deposition AA-CVD

In a typical deposition of the thin films, 0.25 g, 0.435 mmol of **1** was dissolved in THF (20 ml). A quartz tube reactor containing borosilicate glass substrates (1.8 cm × 1.5 cm × 1 mm thick) was placed in a pre-warmed Carbolite furnace. The precursor solution was aerosolized using an ultrasonic humidifier, and the aerosol droplets were carried to the reactor tube by a constant flow of argon (140 cm<sup>3</sup> min<sup>-1</sup>).

#### Results and discussion

Diphenyltin bis(2-methoxyethylxanthate) [Ph<sub>2</sub>Sn(S<sub>2</sub>CO(CH<sub>2</sub>)<sub>2</sub>OMe)<sub>2</sub>] (**1**, Fig. 1a) and diphenyltin bis(*iso*-butylxanthate) [Ph<sub>2</sub>Sn(S<sub>2</sub>CO<sup>*i*</sup>Bu)<sub>2</sub>] (**2**, Fig. 1b) were synthesized from the reaction of the corresponding potassium xanthate [43] and diphenyltin dichloride. The free sulfur atoms do not appear to interact with other atoms in the packed structure (ESI Figures S1.1 and S1.2). In **1**, the Sn center adopts a distorted tetrahedral arrangement, with Ph–Sn–Ph bond angles of 140.0(2)°–144.2(2)°, S–Sn–S of 86.29(5)°–86.34(5)° and S–Sn–C of 100.6(2)°–104.0(2)°. The Sn–S bond lengths are 2.503(1)–2.543(2) Å, while the non-bonding Sn–S distances are 2.914(1)–3.093(2) Å. Complex **2** adopts an analogous distorted tetrahedral arrangement around the tin center with Ph–Sn–Ph bond angles of 146.7(2)°, S–Sn–S of 86.10(5)° and S–Sn–C of

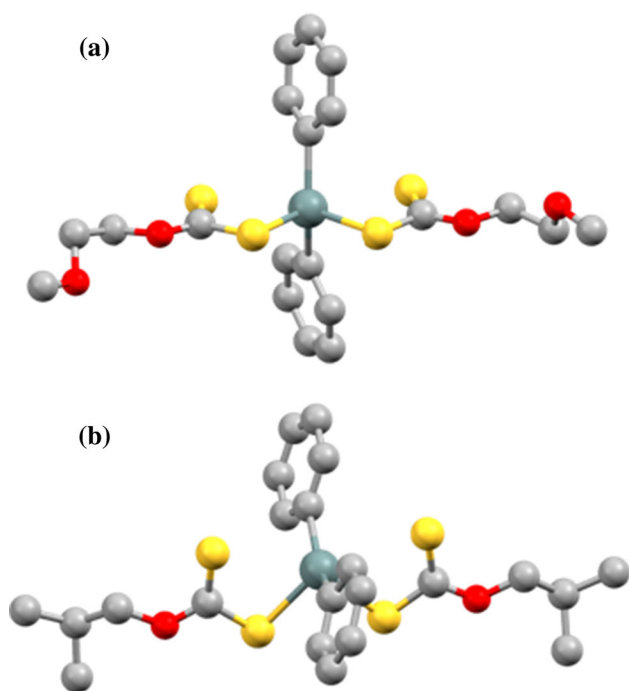


**Figure 1** The structure of **a** diphenyltin bis(2-methoxyethylxanthate) [ $\text{Ph}_2\text{Sn}(\text{S}_2\text{CO}(\text{CH}_2)_2\text{OMe})_2$ ] (**1**) and **b** diphenyltin bis(*iso*-butylxanthate) [ $\text{Ph}_2\text{Sn}(\text{S}_2\text{CO}^i\text{Bu})_2$ ] (**2**). H are omitted for clarity. Teal = Sn, yellow = S, red = O, gray = C.

$101.8(1)^\circ$ – $102.6(1)^\circ$ . It also has similar Sn–S bond lengths to **1** of  $2.5065(7)$ – $2.5134(7)$  Å.

The decomposition of **1** was studied using thermogravimetric analysis (TGA) in the temperature range of  $30$ – $600$  °C at a heating rate of  $10$  °C  $\text{min}^{-1}$  under nitrogen flow. The TGA trace for **1** (ESI

Figure S2.1) shows a clean, one-step decomposition to SnS, with decomposition occurring between  $300$  and  $375$  °C. In contrast, **2** undergoes a two-step decomposition to SnS. Metal xanthates typically decompose via the Chugaev elimination mechanism [48], the first step of which involves elimination of the pendant alkyl groups, followed by carbonyl sulfide. The first step of the decomposition of **2** likely involves elimination of 2 equiv. *isobutylene* and 1 equiv. carbonyl sulfide. The second step would then involve the final loss of the remaining carbonyl sulfide and then aromatic groups. Further investigations will focus on the exact mechanism of decomposition of diaryltin(IV) xanthates.

We used a solution of **1** in THF in an aerosol-assisted chemical vapor deposition (AA-CVD) reactor to generate thin films at temperatures ranging from  $400$  to  $575$  °C under an inert atmosphere of Ar. The grazing incidence X-ray diffraction (GIXRD) patterns of the films (Fig. 2a) indicate that at low temperature tetragonal  $\text{SnO}_2$  (JCPDS 01-070-4177) dominates, but at high temperatures orthorhombic SnS (JCPDS 00-039-0354) is the major species. The GIXRD patterns indicate that at high temperatures some  $\text{SnO}_2$  is still present, and likewise at low temperature there is still some SnS.

Scanning electron microscopy (SEM) reveals that there is a distinct change in morphology as the deposition temperature is increased (Fig. 3). The particles change from a collection of  $0.5$  μm cubes to sheets made of thin rods via thin ( $\sim 100$  nm) sheets

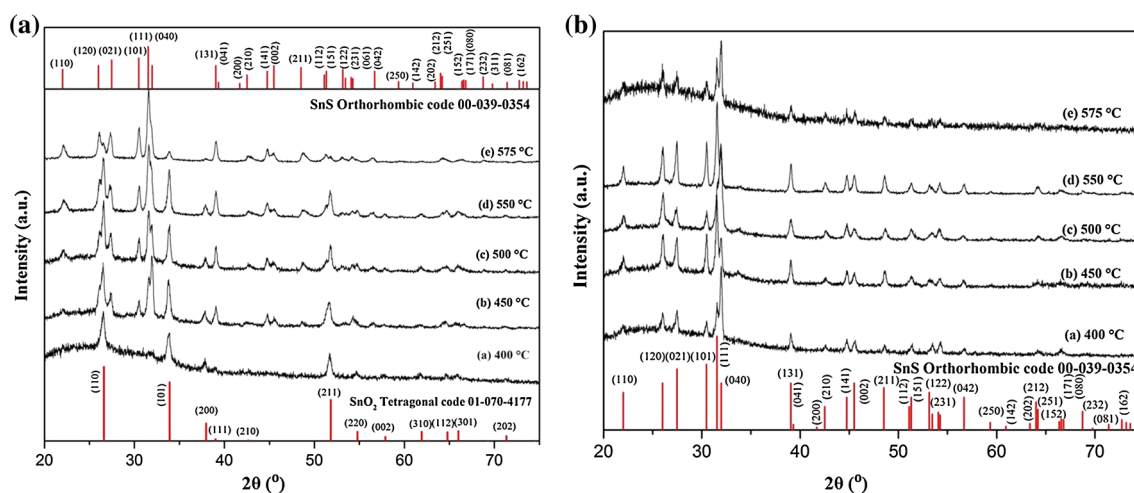


**Figure 2 a** The GIXRD patterns of the obtained films from **1** indicate that tetragonal  $\text{SnO}_2$  dominates at low temperatures, but orthorhombic SnS is the major phase at high temperatures. Note

that there is still some  $\text{SnO}_2$  present at high temperatures and some SnS at low temperatures. **b** The GIXRD patterns of films obtained from **2** indicate clean formation of SnS at all temperatures.



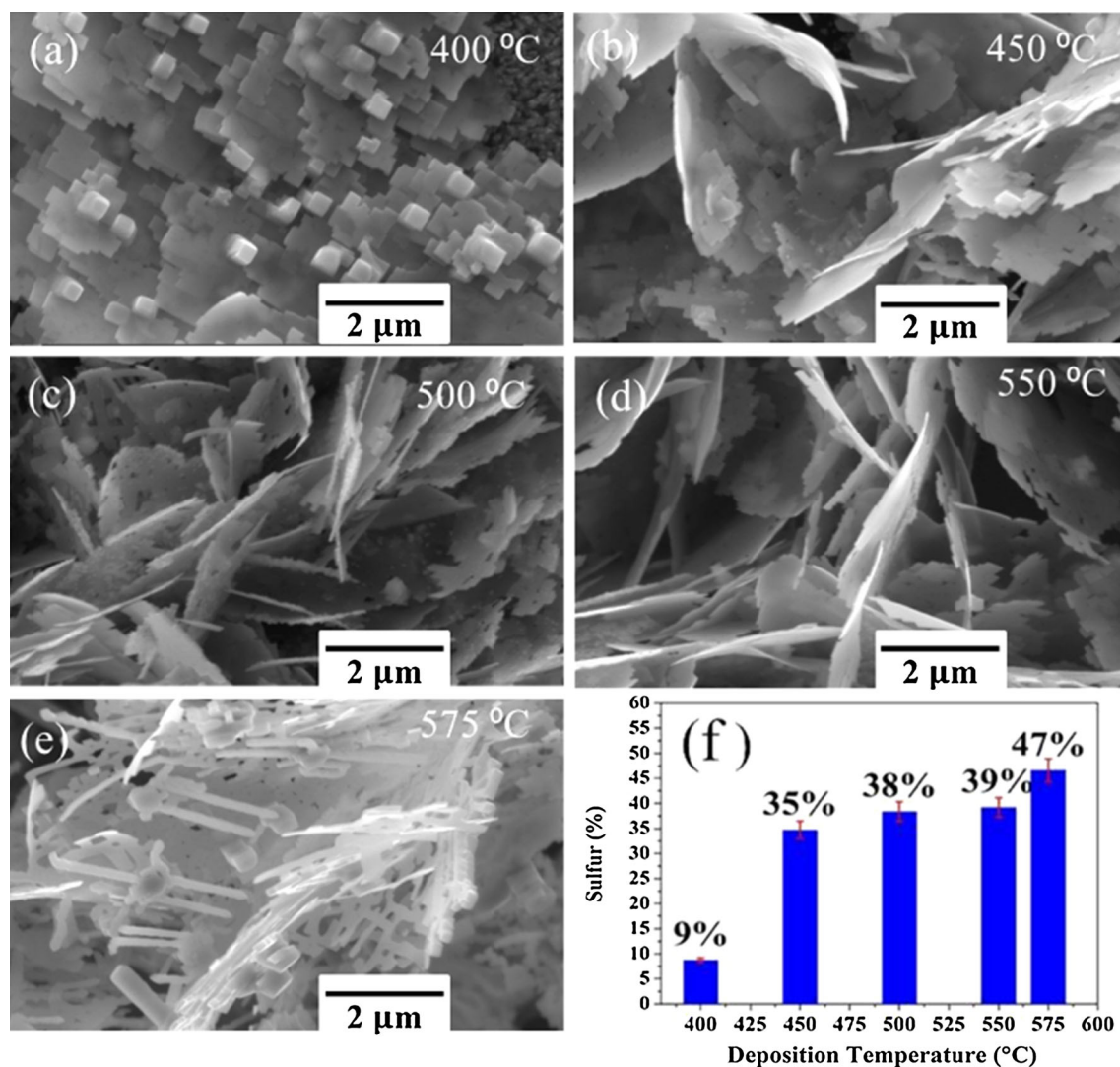


**Figure 3** a–e Scanning electron microscopy (SEM) images of the deposited films. f Sulfur content determined by energy-dispersive X-ray spectroscopy (EDX).

(Fig. 3). The sulfur composition was determined by energy-dispersive X-ray spectroscopy (EDX, Fig. 3f), and this indicates an increased S content as the reaction temperature is increased. This is in agreement with the GIXRD patterns, which show an analogous transition from  $\text{SnO}_2$  to  $\text{SnS}$ .

Samples suitable for transmission electron microscopy (TEM) imaging were prepared by ultrasonication of the films deposited at 400 and 575 °C from complex 1. In order to examine the material at higher resolution, high-angle annular dark-field (HAADF) scanning transmission electron microscope (STEM) imaging and STEM-EDX spectrum imaging were used. The microscopy reveals the presence of a possible  $\text{SnS}/\text{SnO}_2$  lateral heterojunction in the material

prepared at 575 °C. In Fig. 4a, we show the HAADF STEM image of a sample prepared at 575 °C, which reveals contrasting brighter and darker regions. The EDX maps shown in Fig. 4b–e indicate that the bright regions are oxygen rich, while the darker regions are S rich. An EDX line scan (ESI Figure S3.1) indicates that the S and O are mutually exclusive, with a very sharp transition from  $\text{SnS}$  to  $\text{SnO}_2$ . It is apparent in this case that the orthorhombic  $\text{SnS}$  and tetragonal  $\text{SnO}_2$  are present in the same flake. Atomic resolution TEM images (ESI Figure S3.2) of the material provide further evidence of sharp interfaces between regions of crystalline  $\text{SnS}$  and  $\text{SnO}_2$ .

In contrast to this, in the sample prepared at 400 °C it appears that  $\text{SnO}_2$  particles decorate the surface of

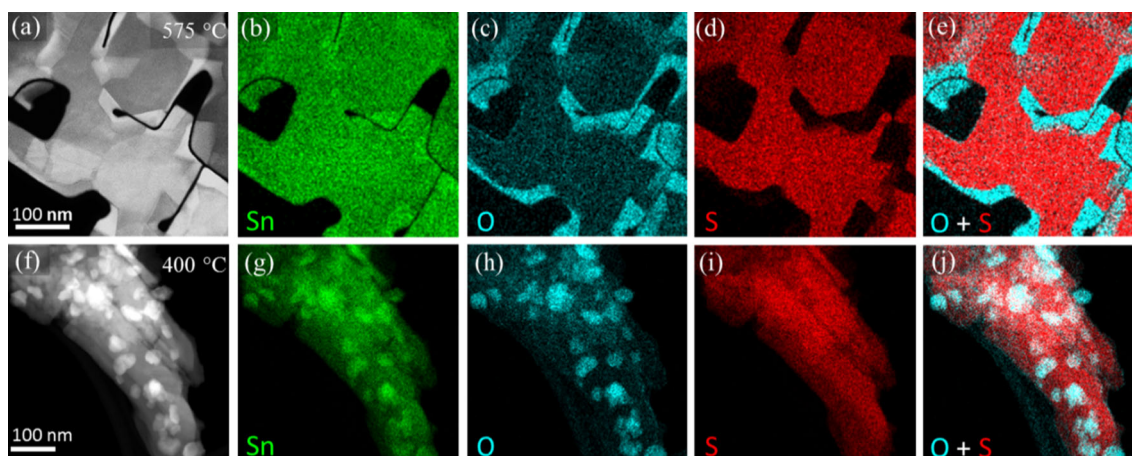


**Figure 4** STEM EDX spectrum imaging of samples prepared at 575 °C (a–e) and 400 °C (f–j). HAADF STEM images of the mapped regions are shown on the far left with corresponding EDX

maps for Sn, O and S going from left to right; overlaid maps of O and S counts are found on the far right.

the SnS crystals (Fig. 4f–j). Note that SnS has a density of  $5.22 \text{ g cm}^{-3}$ , while  $\text{SnO}_2$  has a density of  $6.95 \text{ g cm}^{-3}$ ; it is therefore unsurprising that oxide regions appear brighter in HAADF images (Fig. 4f). The sample has a clearly different morphology, appearing much less flake like in the SEM than the other samples (Fig. 3).

The Chugaev elimination usually gives the relevant metal sulfide in a clean manner, with zero O contamination/content [44, 48, 50–54]. We investigated the reason for the presence of  $\text{SnO}_2$  in these products through the synthesis and decomposition of a second diorganotin(IV) xanthate, diphenyltin bis(*iso*-butylxanthate) (**2**, Fig. 1b). **2** was used in the AA-CVD apparatus in exactly the same manner as **1**, but in this case the GIXRD pattern indicates that SnS is the only product (Fig. 2b). This result clearly implies that the second oxygen in the xanthate chain of **1** must be key to the production of  $\text{SnO}_2$  under the anaerobic conditions of deposition. Therefore, we tentatively suggest that metal alkoxyxanthates of the type  $[\text{M}(\text{S}_2\text{CO}(\text{CH}_2)_2\text{OR})_x]$  are a class of compound that is worth further exploration as they may yield interesting and complex  $\text{MS}_x:\text{MO}_y$  lateral heterojunctions. Alternatively, if seeking to avoid oxide formation, it is clear that the xanthato oxygen is not a problem, but other O atoms further down the alkyl chain are. Future work will look into the ability to fabricate heterostructures from a single molecular precursor: the potential to control both the chemical composition and morphology of the products through

reaction temperature is an attractive proposition, especially considering the simplicity and potential scalability of AA-CVD.

The optical band gaps ( $E_g$ ) of the films were calculated by from Tauc plots (ESI Table S5.1, ESI Figures S5.1 and S5.2). For the films deposited from complex **1**, the band gap of the films deposited at 400 °C is 2.97 eV, while increasing the deposition temperature resulted in a decrease in  $E_g$ : 2.91 eV (450 °C), 2.60 (500 °C), 2.47 (550 °C) and 1.71 eV (575 °C).  $\text{SnO}_2$  is predicted to have direct energy gap of 3.68 eV [55, 56], and SnS has a direct band gap of 1.32 eV [57]. The control of the stoichiometry that we have obtained in the syntheses of the films allows for tuning of band gaps. Films deposited from complex **2** gave pure phase SnS, and the experimentally determined band gaps match the literature values well, with  $E_g$  for the films formed at 500, 550 and 575 °C of 1.46, 1.41 and 1.28 eV, respectively.

## Conclusions

In conclusion, we have reported the synthesis of SnS thin films and SnS/ $\text{SnO}_2$  nanocomposite from diorganotin(IV) dioxanthate complexes. We have discovered that including a second oxygen in the alkyl chain of the xanthate can be used to introduce an certain amount of oxide formation, with the stoichiometry being controllable through deposition temperature. The method that we have presented

here is simple and easily scalable, which we hope will encourage the use of this exciting material. We believe that this control over the stoichiometry of oxide to chalcogenide may be of use to researchers looking at other metal chalcogenides/oxides, with the potential for synthesizing lateral heterostructures. This could access exciting functionality and thus increase the abilities of future devices.

## Acknowledgements

The authors would like to acknowledge the Iraqi Culture Attaché in London and Department of Physics, College of Science, University of Misan, Iraq, for financial support (M.A.S.) and the EPSRC (Doctoral Prize for E.A.L., Grant EP/M507969/1). Some of the equipments used in this study were provided by the Engineering and Physical Sciences Research Council (Core Capability in Chemistry, EPSRC Grant Number EP/K039547/1). P.D.M. would like to acknowledge the UK Government and European Union as contributors to the Smart Energy Network Demonstrator (ERDF Project Number 32R16P00706).

## Compliance with ethical standards

**Conflict of interest** The authors declare that they have no conflict of interest.

**Electronic supplementary material:** The online version of this article (<https://doi.org/10.1007/s10853-018-2968-y>) contains supplementary material, which is available to authorized users.

**Open Access** This article is distributed under the terms of the Creative Commons Attribution 4.0 International License (<http://creativecommons.org/licenses/by/4.0/>), which permits unrestricted use, distribution, and reproduction in any medium, provided you give appropriate credit to the original author(s) and the source, provide a link to the Creative Commons license, and indicate if changes were made.

## References

- [1] Tedstone AA, Lewis DJ, O'Brien P (2016) Synthesis, properties and applications of transition metal-doped layered transition metal dichalcogenides. *Chem Mater* 28:1965–1974. <https://doi.org/10.1021/acs.chemmater.6b00430>
- [2] Li BL, Setyawati MI, Chen L et al (2017) Directing assembly and disassembly of 2D MoS<sub>2</sub> nanosheets with DNA for drug delivery. *ACS Appl Mater Interfaces* 9:15286–15296. <https://doi.org/10.1021/acsami.7b02529>
- [3] Chen W, Qu Y, Yao L et al (2018) Electronic, magnetic, catalytic, and electrochemical properties of two-dimensional Janus transition metal chalcogenides. *J Mater Chem A* 6:8021–8029. <https://doi.org/10.1039/c8ta01202d>
- [4] Chhowalla M, Liu Z, Zhang H (2015) Two-dimensional transition metal dichalcogenide (TMD) nanosheets. *Chem Soc Rev* 44:2584–2586. <https://doi.org/10.1039/c5cs90037a>
- [5] Matthews PD, McNaughton PD, Lewis DJ, O'Brien P (2017) Shining a light on transition metal chalcogenides for sustainable photovoltaics. *Chem Sci* 8:4177–4187. <https://doi.org/10.1039/C7SC00642J>
- [6] Chao D, Liang P, Chen Z et al (2016) Pseudocapacitive Na-Ion storage boosts high rate and areal capacity of self-branched 2D layered metal chalcogenide nanoarrays. *ACS Nano* 10:10211–10219. <https://doi.org/10.1021/acs.nano.6b05566>
- [7] Nie L, Zhang Q (2017) Recent progress in crystalline metal chalcogenides as efficient photocatalysts for organic pollutant degradation. *Inorg Chem Front* 4:1953–1962. <https://doi.org/10.1039/c7qi00651a>
- [8] Wang H, Yuan H, Hong SS et al (2015) Physical and chemical tuning of two-dimensional transition metal dichalcogenides. *Chem Soc Rev* 44:2664–2680. <https://doi.org/10.1039/c4cs00287c>
- [9] Han JH, Kwak M, Kim Y, Cheon J (2018) Recent advances in the solution-based preparation of two-dimensional layered transition metal chalcogenide nanostructures. *Chem Rev* 118:6151–6188. <https://doi.org/10.1021/acs.chemrev.8b00264>
- [10] Jariwala D, Sangwan VK, Lauhon LJ et al (2014) Emerging device applications for semiconducting two-dimensional transition metal dichalcogenides. *ACS Nano* 8:1102–1120. <https://doi.org/10.1021/nn500064s>
- [11] Pumera M, Sofer Z, Ambrosi A (2014) Layered transition metal dichalcogenides for electrochemical energy generation and storage. *J Mater Chem A* 2:8981–8987. <https://doi.org/10.1039/c4ta00652f>
- [12] Chia X, Pumera M (2018) Layered transition metal dichalcogenide electrochemistry: journey across the periodic



- table. *Chem Soc Rev* 47:5602–5613. <https://doi.org/10.1039/c7cs00846e>
- [13] Gao Y-P, Wu X, Huang K-J et al (2017) Two-dimensional transition metal diseleniums for energy storage application: a review of recent developments. *CrystEngComm* 19:404–418. <https://doi.org/10.1039/C6CE02223E>
- [14] Ramakrishna Reddy KT, Koteswara Reddy N, Miles RW (2006) Photovoltaic properties of SnS based solar cells. *Sol Energy Mater Sol Cells* 90:3041–3046. <https://doi.org/10.1016/j.solmat.2006.06.012>
- [15] Lewis DJ, Kevin P, Bakr O et al (2014) Routes to tin chalcogenide materials as thin films or nanoparticles: a potentially important class of semiconductors for sustainable solar energy conversion. *Inorg Chem Front* 1:577–598. <https://doi.org/10.1039/C4QI00059E>
- [16] Sinsermsuksakul P, Sun L, Lee SW et al (2014) Overcoming efficiency limitations of SnS-based solar cells. *Adv Energy Mater* 4:1400496. <https://doi.org/10.1002/aenm.201400496>
- [17] Vaughn DD, Hentz OD, Chen S et al (2012) Formation of SnS nanoflowers for lithium ion batteries. *Chem Commun* 48:5608–5610. <https://doi.org/10.1039/c2cc32033a>
- [18] Burton LA, Colombara D, Abellon RD et al (2013) Synthesis, characterization, and electronic structure of single-crystal SnS, Sn<sub>2</sub>S<sub>3</sub>, and SnS<sub>2</sub>. *Chem Mater* 25:4908–4916. <https://doi.org/10.1021/cm403046m>
- [19] Brent JR, Lewis DJ, Lorenz T et al (2015) Tin(II) sulfide (SnS) nanosheets by liquid-phase exfoliation of herzenbergite: IV–VI main group two-dimensional atomic crystals. *J Am Chem Soc* 137:12689–12696. <https://doi.org/10.1021/jacs.5b08236>
- [20] Matthews PD, Hirunpinyopas W, Lewis EA et al (2018) Black phosphorus with near-superhydrophobic properties and long-term stability in aqueous media. *Chem Commun* 54:3831–3834. <https://doi.org/10.1039/c8cc01789a>
- [21] Burton LA, Walsh A (2012) Phase stability of the earth-abundant tin sulfides SnS, SnS<sub>2</sub>, and Sn<sub>2</sub>S<sub>3</sub>. *J Phys Chem C* 116:24262–24267. <https://doi.org/10.1021/jp309154s>
- [22] Bade BP, Garje SS, Niwate YS et al (2008) Tribenzyltin(IV)chloride thiosemicarbazones: novel single source precursors for growth of SnS thin films. *Chem Vap Depos* 14:292–295. <https://doi.org/10.1002/cvde.200806687>
- [23] Kevin P, Lewis DJ, Raftery J et al (2015) Thin films of Tin(II) sulphide (SnS) by aerosol-assisted chemical vapour deposition (AACVD) using Tin(II) dithiocarbamates as single-source precursors. *J Cryst Growth* 415:93–99. <https://doi.org/10.1016/j.jcrysgro.2014.07.019>
- [24] Barone G, Hibbert T, Mahon M et al (2001) Deposition of tin sulfide thin films from tin(IV) thiolate precursors. *J Mater Sci*. <https://doi.org/10.1039/b005888m>
- [25] Hibbert TG, Mahon MF, Molloy KC et al (2001) Deposition of tin sulfide thin films from novel, volatile (fluoroalkylthiolato)tin(IV) precursors. *J Mater Chem* 11:469–473. <https://doi.org/10.1039/b005863g>
- [26] Ramasamy K, Kuznetsov VL, Gopal K et al (2013) Organotin dithiocarbamates: single-source precursors for tin sulfide thin films by aerosol-assisted chemical vapor deposition (AACVD). *Chem Mater* 25:266–276. <https://doi.org/10.1021/cm301660n>
- [27] Ahmet IY, Hill MS, Johnson AL, Peter LM (2015) Polymorph-selective deposition of high purity SnS thin films from a single source precursor. *Chem Mater* 27:7680–7688. <https://doi.org/10.1021/acs.chemmater.5b03220>
- [28] Al-Shakban M, Xie Z, Savjani N et al (2016) A facile method for the production of SnS thin films from melt reactions. *J Mater Sci* 51:6166–6172. <https://doi.org/10.1007/s10853-016-9906-7>
- [29] Koteeswara Reddy N, Devika M, Ahsanulhaq Q, Gunasekhar KR (2010) Growth of orthorhombic SnS nanobox structures on seeded substrates. *Cryst Growth Des* 10:4769–4772. <https://doi.org/10.1021/cg100621d>
- [30] Gao C, Shen H (2012) Influence of the deposition parameters on the properties of orthorhombic SnS films by chemical bath deposition. *Thin Solid Films* 520:3523–3527. <https://doi.org/10.1016/j.tsf.2011.12.077>
- [31] Greyson EC, Barton JE, Odom TW (2006) Tetrahedral zinc blende tin sulfide nano- and microcrystals. *Small* 2:368–371. <https://doi.org/10.1002/smll.200500460>
- [32] Herron SM, Tanskanen JT, Roelofs KE, Bent SF (2014) Highly textured tin(II) sulfide thin films formed from sheetlike nanocrystal inks. *Chem Mater* 26:7106–7113. <https://doi.org/10.1021/cm503666y>
- [33] Rabkin A, Samuha S, Abutbul RE et al (2015) New nanocrystalline materials: a previously unknown simple cubic phase in the SnS binary system. *Nano Lett* 15:2174–2179. <https://doi.org/10.1021/acs.nanolett.5b00209>
- [34] Steinmann V, Jaramillo R, Hartman K et al (2014) 3.88% efficient tin sulfide solar cells using congruent thermal evaporation. *Adv Mater* 26:7488–7492. <https://doi.org/10.1002/adma.201402219>
- [35] Devika M, Ramakrishna Reddy KT, Koteeswara Reddy N et al (2006) Microstructure dependent physical properties of evaporated tin sulfide films. *J Appl Phys* 100:23518. <https://doi.org/10.1063/1.2216790>
- [36] Tian Z, Guo C, Zhao M et al (2017) Two-dimensional SnS: a phosphorene analogue with strong in-plane electronic anisotropy. *ACS Nano* 11:2219–2226. <https://doi.org/10.1021/acsnano.6b08704>
- [37] Steichen M, Djemour R, Gütay L et al (2013) Direct synthesis of single-phase p-type SnS by electrodeposition from a



- dicyanamide ionic liquid at high temperature for thin film solar cells. *J Phys Chem C* 117:4383–4393. <https://doi.org/10.1021/jp311552g>
- [38] Mathews NR, Anaya HBM, Cortes-Jacome MA et al (2010) Tin sulfide thin films by pulse electrodeposition: structural, morphological, and optical properties. *J Electrochem Soc* 157:H337–H341. <https://doi.org/10.1149/1.3289318>
- [39] Boudjouk P, Seidler DJ, Grier D, McCarthy GJ (1996) Benzyl-substituted tin chalcogenides. efficient single-source precursors for tin sulfide, tin selenide, and  $\text{Sn}(\text{S}_x\text{Se}_{1-x} < i / > )$  solid solutions. *Chem Mater* 8:1189–1196. <https://doi.org/10.1021/cm9504347>
- [40] Al-Shakban M, Matthews PD, O'Brien P (2017) A simple route to complex materials: the synthesis of alkaline earth—transition metal sulfides. *Chem Commun* 53:10058–10061. <https://doi.org/10.1039/C7CC05643E>
- [41] Al-Shakban M, Matthews PD, Zhong XL et al (2018) On the phase control of  $\text{CuInS}_2$  nanoparticles from Cu-/In-xanthates. *Dalton Trans* 47:5304–5309. <https://doi.org/10.1039/C8DT00653A>
- [42] Matthews PD, Akhtar M, Malik MA et al (2016) Synthetic routes to iron chalcogenide nanoparticles and thin films. *Dalton Trans* 45:18803–18812. <https://doi.org/10.1039/C6DT03486A>
- [43] Al-Shakban M, Matthews PD, Deogratias G et al (2017) Novel xanthate complexes for the size controlled synthesis of copper sulfide nanorods. *Inorg Chem* 56:9247–9254
- [44] Al-Shakban M, Matthews PD, Savjani N et al (2017) The synthesis and characterization of  $\text{Cu}_2\text{ZnSnS}_4$  thin films from melt reactions using xanthate precursors. *J Mater Sci* 52:12761–12771. <https://doi.org/10.1007/s10835-017-1367-0>
- [45] Lewis EA, McNaughten PD, Yin Z et al (2015) In situ synthesis of  $\text{PbS}$  nanocrystals in polymer thin films from lead(II) xanthate and dithiocarbamate complexes: evidence for size and morphology control. *Chem Mater* 27:2127–2136. <https://doi.org/10.1021/cm504765z>
- [46] Kana AT, Hibbert TG, Mahon MF et al (2001) Organotin unsymmetric dithiocarbamates: synthesis, formation and characterisation of tin(II) sulfide films by atmospheric pressure chemical vapour deposition. *Polyhedron* 20:2989–2995. [https://doi.org/10.1016/S0277-5387\(01\)00908-1](https://doi.org/10.1016/S0277-5387(01)00908-1)
- [47] Afzaal M, Rosenberg CL, Malik MA et al (2011) Phosphine stabilized copper(I) complexes of dithiocarbamates and xanthates and their decomposition pathways. *New J Chem* 35:2773–2780. <https://doi.org/10.1039/c1nj20586b>
- [48] Buckingham MA, Catherall AL, Hill MS et al (2017) Aerosol-assisted chemical vapor deposition of  $\text{CdS}$  from xanthate single source precursors. *Cryst Growth Des* 17:907–912. <https://doi.org/10.1021/acs.cgd.6b01795>
- [49] Edwards AJ, Hoskins BF, Winter G (1988) Structure of triphenyltin(IV) methoxyethylxanthate. *Acta Cryst C* 44:1541–1543. <https://doi.org/10.1107/S0108270188005463>
- [50] Akhtar J, Afzaal M, Vincent MA et al (2011) Low temperature CVD growth of  $\text{PbS}$  films on plastic substrates. *Chem Commun* 47:1991–1993. <https://doi.org/10.1039/c0cc05036a>
- [51] Clark JM, Kociok-Köhn G, Harnett NJ et al (2011) Formation of  $\text{PbS}$  materials from lead xanthate precursors. *Dalton Trans* 40:6893–6900. <https://doi.org/10.1039/c1dt10273g>
- [52] McNaughten PD, Saah SA, Akhtar M et al (2016) lead(II) xanthates and their decomposition to  $\text{PbS}$  in melt reactions. *Dalton Trans* 45:16345–16353. <https://doi.org/10.1039/c6dt02859d>
- [53] Rath T, MacLachlan AJ, Brown MD, Haque SA (2015) Structural, optical and charge generation properties of chalcocite and tetrahedrite copper antimony sulfide thin films prepared from metal xanthates. *J Mater Chem A* 3:24155–24162. <https://doi.org/10.1039/C5TA05777A>
- [54] Lutz T, MacLachlan A, Sudlow A et al (2012) Thermal decomposition of solution processable metal xanthates on mesoporous titanium dioxide films: a new route to quantum-dot sensitised heterojunctions. *Phys Chem Chem Phys* 14:16192–16196. <https://doi.org/10.1039/c2cp43534a>
- [55] Arlinghaus FJ (1974) Energy bands in stannic oxide ( $\text{SnO}_2$ ). *J Phys Chem Solids* 35:931–935. [https://doi.org/10.1016/S0022-3697\(74\)80102-2](https://doi.org/10.1016/S0022-3697(74)80102-2)
- [56] Ganose AM, Scanlon DO (2016) Band gap and work function tailoring of  $\text{SnO}_2$  for improved transparent conducting ability in photovoltaics. *J Mater Chem C* 4:1467–1475. <https://doi.org/10.1039/C5TC04089B>
- [57] Reddy NK, Reddy KTR (1998) Growth of polycrystalline  $\text{SnS}$  films by spray pyrolysis. *Thin Solid Films* 325:4–6. [https://doi.org/10.1016/S0040-6090\(98\)00431-3](https://doi.org/10.1016/S0040-6090(98)00431-3)